Development of a MHz Pulsed Power Supply for Kicker Magnet in SHINE

Yong-Fang Liu, *Member, IEEE*, Ming Gu, Qi-Bing Yuan, Ruiping Wang, Jin Tong, and Sheying Li

***Abstract*—Shanghai high repetition rate X-ray free electron laser and extreme light (SHINE) project is a superconducting linear electron accelerator-based facility under construction at the Shanghai Advance Research Institute, Chinese Academy of Sciences. It provides electron beam bunches with an energy of 8 GeV and requires a beam distribution system to switch at a repetition rate of 1 MHz between three undulator lines and a dump. This article presents the unique challenges of designing a pulsed power supply for the kicker magnet in the SHINE facility at a high repetition of 1 MHz. A fast pulse forming topology on the basis of inductor, resistor, and capacitor second-order circuit aiming for a kicker magnet was proposed. The mathematical models of the peak current of the kicker magnet, time transient at the peak current were derivated, and subsequently applied to determine the key parameters in the circuit design. Experimental results demonstrate a pulse-to-pulse amplitude stability of 108 ppm, a pulse width less than 1 μs and a peak current of ∼44.1 A at a repetition rate of 1 MHz. These findings are in corresponding to the design parameters proposed for the project.**

***Index Terms*—Beam distribution system, high repetition rate, pulsed power supply, pulse-to-pulse stability, X-ray free electron laser.**

I. Introduction

THE X-ray free electron laser (XFEL) facility based on a linear electron accelerator (linac) has exhibited high coherence and light intensity, short pulses (in the order of a few μs), as well as tunability [1], [2], [3]. The facility is anticipated to be exploited for revolutionary scientific experiments in a variety of disciplines spanning physics, chemistry, biology, and materials science. Several XFEL facilities have been reported. Swiss XFEL (SwissFEL) developed at the Paul Scherrer Institute [4] and Japanese XFEL [SPring-8 Angstrom Compact Free-Electron Laser (SACLA)] developed at RIKEN SPring-8 Center [5], [6] are linac-based XFEL facilities that have been used for scientific research.

Manuscript received 13 September 2023; revised 23 November 2023; accepted 21 December 2023. Date of publication 28 December 2023; date of current version 16 February 2024. This work was supported in part by the Shanghai Municipal Science and Technology Major Project under Grant 2017SHZDZX02, in part by the National Natural Science Foundation of China under Grant 12005282, and in part by Youth Innovation Promotion Association of Chinese Academy of Sciences under Grant 2021283. Recommended for publication by Associate Editor A. Safaee. *(Corresponding author: Sheying Li.)*

The authors are with the Shanghai Advanced Research Institute, Chinese Academy of Sciences, Shanghai 201412, China (e-mail: liuyongfang@sari.ac.cn; gum@sari.ac.cn; yuanqb@sari.ac.cn; wangrp@sari.ac.cn; tongj.@sari.ac.cn; lisheying@sari.ac.cn).

Color versions of one or more figures in this article are available at https://doi.org/10.1109/TPEL.2023.3347748.

Digital Object Identifier 10.1109/TPEL.2023.3347748

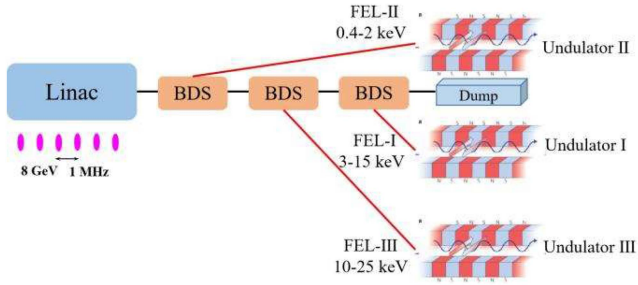

Fig. 1. Schematic view of the branching of electron beam-lines through the beam distribution systems and undulators in SHINE.

The European XFEL (EXFEL) [1], [7], [8] and LCLS-II [9] underlie the superconducting linac technology for multiexperimental users. The Shanghai High repetition rate X-ray free electron laser (XFEL) and Extreme Light (SHINE) is a superconducting linac-based facility under construction at the Shanghai Advance Research Institute (SARI), Chinese Academy of Sciences [3], [10], aiming for construction from 2018–2025. The crucial components of the facility are composed of injector, linac, beam distribution system (BDS), undulators, photon beamlines, and instruments in the experimental stations. These devices are disposed of in a linear geometry ∼30 m underground with a total length of up to 3.1 km - spanning the Shanghai Synchrotron Radiation Facility and Soft XFEL campuses. Briefly, electron bunches are extracted from a solid cathode via a laser beam in the injector, accelerated by an electron radio frequency gun, and directed towards the linac at an exit energy of 100 MeV. Subsequently, they are further accelerated in the linac—consisting of 1.4 km of superconducting accelerating modules, magnets for beam steering and focusing, and diagnostic instruments—to an energy of up to 8 GeV at a frequency of 1 MHz. It is based on a linac with maximum energy of 8 GeV, at a maximum repetition rate of 1 MHz, as shown in Fig. 1. The BDS in SHINE directs the individual electron beam bunches to each of the undulator lines at the end of linac. Electron beam bunches channeled down the electron bean bunches through the undulators, generating X-ray photons with varied energy—FEL-I (3–15 keV), FEL-II (0.4–2 keV), and FEL-III (10–25 keV)—as indicated in Fig. 1. The photons produced by the undulators are then transported via the respective photon beam lines to the experimental stations.

To improve the operating efficiency of the facility, the BDS is capable of directing individual beam bunches to the undulator lines through different sets of kicker and septum magnet,

TABLE I
SUMMARY OF SPECIFICATIONS OF THE KICKER MAGNETS FOR XFEL FACILITIES

Para. \ Facilities	SACLA	SwissFEL	EXFEL	LCLS-II	SHINE
Load	Inductor, 16 mH	Inductor, 380 nH	Resistor, 50–60 Ω	Resistor, 12.5 Ω	Inductor, 1.25 μH
Electron beam energy	7 GeV	3 GeV	20 GeV	4 GeV	8 GeV
Repetition rate	60 Hz	100 Hz	5 MHz, 10 Hz	~929 kHz	1 MHz
Pulsed current	±300 A	±600 A	Flat-top current ~250 A	66 A	≥42 A
Kicker type	Bending magnet	Resonant kicker magnet	Strip-line	Transmission line magnet	Lumped inductance
Pulsed power supply	LC resonance oscillation	High Q-factor resonant deflecting magnet	MOSFET chopped wave	MOSFET chopped wave	MOSFET chopped wave
Pulse-to-pulse amplitude stability	< 0.003%	±0.001%	1%@ 5 MHz 0.01%@ 10 Hz	0.01%	0.01%
Ref.	[5]	[4], [11], [12]	[7], [11]	[9]	[10]

enabling the use of many experimental stations by varied users simultaneously. Fast switching between the undulator lines is required within a bunch train to fully utilize the available beam. Additionally, the bunch repetition pattern can be adjusted individually to adapt each undulator line. This is achieved via the combinations of the kicker-septum, distributing bunches towards each undulator line or into a beam dump as desired. Pulsed power supply is the key element to provide the required pulsed excitation current power for the kicker magnet (load in this case). Traditionally, the beam bunches repetition rate for the linac is constrained within 100 Hz [1]. Nevertheless, a superconducting linac generates electron bunches with much higher energy at a frequency in the order of Megahertz (MHz) [1].

An overview of the existing kicker magnets for the XFEL facilities worldwide is provided in Table I for further comparison. As aforementioned, SACLA and SwissFEL are linac-based X-ray FEL facilities, while the other three superconducting linac-based facilities are EXFEL, LCLS-II, and SHINE. As a key element in directing the beam bunches to desired undulator lines, the design of pulsed power supply is discussed in detail. Referring to Table I, in SACLA, a pulsed power supply based on inductor, capacitor (*LC*) inductance resonances was designed, exhibiting an output power of 0.3 MW (300 A and 1 kV) with a stability of 10 ppm [6]. It was capable of generating bipolar trapezoidal current waveform at a repetition rate of 60 Hz. A resonant pulsed power supply in SwissFEL was designed for a pulse current up to 600 A at a repetition rate of 100 Hz [12].

Here, the focus relies on the latter three infrastructures that are based on superconducting linac technologies. As indicated in Table I, two types of kicker pulsed power supply are used in EXFEL. A fast kicker pulsed power supply based on a fast high voltage switch (Behlke HTS 80-12-UF) operates at a repetition rate of 5 MHz with a required relative amplitude stability of 1% (beam bunches dumped). While a flat-top kicker power supply based on a capacitor array (0.2 F) - charged by a dc power supply and discharged via a fast insulated-gate bipolar transistor (IGBT) switch—operates at a frequency of 10 Hz with required relative amplitude stability of 0.01% [7], [11]. In LCLS-II, a superconducting linac generates 4 GeV electron beam bunches at a repetition rate of 929 kHz, and then transported to the photon beam lines between a soft X-ray undulator line, a hard X-ray undulator line, and a beam dump [9]. A ferrite-loaded transmission line kicker magnet topology was adopted due to the required high voltage (~900 V). Experimental results illustrated the pulse-to-pulse stability of approximately 0.01% at a repetition rate of 500 kHz.

SHINE is the most recently proposed high repetition rate (at 1 MHz) hard X-ray FEL facility that is based on an 8 GeV superconducting acceleration, as shown in Table I. This high repetition rate ensures the rapidly increase of the output power without reducing the single electron charges, and more scientific instruments to be operated in parallel. Pulsed power supply appears to be the crucial element to supply the required pulsed excitation current power for the load (kicker magnet in this case) with a stability of 100 ppm. This high pulse-to-pulse stability is required to maintain the trajectory variation of the electron beam. The proposed indicators—a pulsewidth less than 1 μs, repetition rate of 1 MHz, and stability of 100 ppm—represent the most stringent demands compared to other XFEL facilities (discussed previously). This has posed a significant challenge to the development of the pulsed power supply to fulfill the design criteria of the SHINE facility.

Several pulse forming circuits are commonly used in the pulsed power supply, such as resonant circuits, pulse-forming networks, pulse-forming lines, high-voltage switching chopped-wave, MARX generators, and linear transformer drivers [14], [15], [16], [17]. The electrical energy is mostly accumulated in terms of capacitors (C) over a period and then released in the form of pluses in a short duration for varied power applications. The latter two are widely employed in high-voltage pulsed power applications, which typically charge capacitive and resistive loads and form the basis of many pulse compression schemes. Whereas, when driving the inductive loads, the front-edge of the pulse would be reduced due to the inductance of load. Resonant circuit, transmission line and *LR* chopped-wave circuit are commonly used to generate the pulse schemes for an inductive load. As discussed previously, the resonant circuit and transmission line accumulate energy primarily by charging the transmission lines or capacitors, and then the energy is discharged to the loads in the form of pulses. This process requires a charging and discharging duration over a short period of 1 μs when applied at high reparation rate of 1 MHz. The charging current would be rapidly increased, ultimately affecting the amplitude jitter of the output pulse. For the LR chopped-wave circuit,

the resistance (R) needs to be increased to reduce the time constant as the inductance remains constant (L). As a result, the charging voltage would be raised, which in turn limits the choices of the high-voltage switches. In comparison to traditional silicon-based switches (IGBT, gate turn-OFF thyristor), the most commercially available silicon carbide (SiC) power metal-oxide-semiconductor field-effect transistor (MOSFET) offers a higher voltage rating of approximately 1.7 kV [18], [19], high-frequency operations, and low switching losses. It allows both a large power capacity and a fast-switching speed. Several studies based on the abovementioned methods on the pulsed power supply have been conducted [20], [21], [22], [23]. A high-frequency pulsed power supply based on H-bridge modular topology was designed, which generated pulses amplitudes up to $\pm$10 kV and pulse widths from 500 ns to 5 μs for the biological application [20]. The high pulse frequency at 500 kHz was reached only by the burst mode [20]. Another pulse generator operated at a frequency of 10 MHz and peak voltage amplitude of $<$500 V was developed based on the pulse forming line [21]. The high frequency was achieved by using dual-switch timing logic control, whereas the low voltage amplitude was limited by the turning-ON voltage of the MOSFETs. The waveform was easily affected by the distributed parameters with inductive load owing to the impedance mismatch. It can be seen that the studies are mostly equipped with resistive and capacitive loads, however, the inductive load consecutively operated at a high repetition rate of 1 MHz is rarely investigated.

This article presents the unique challenges—operated at a high repetition rate of 1 MHz, high stability of 0.01% at 8 GeV beam energy, waveform width less than 1 μs, flat-top width of $\sim$5 ns and front-edge time jitter less than 1 ns—of designing a pulsed power supply for the kicker magnets in the SHINE facility. Essentially, several challenges need to be resolved to achieve consecutive operations at such conditions, including i) the busbar voltage stability of $\leq$100 ppm; ii) novel circuit topology to achieve the high driving capability of the MOSFET; iii) prompt stability at an ultrashort time duration of 1 μs; iv) mitigate the influences of the stray inductance of the inductive load. To cope with these technical difficulties, a novel fast pulse forming scheme based on inductor, resistor, and capacitor (*LRC*) second-order circuit aiming for a kicker load was proposed. The formulas of the peak current of the inductor and time transient at the peak current were derivated, and then applied for the guidance of the main parameters in the circuit design. A detailed mathematical analysis of the circuit was examined, while the principal scheme and circuit topology were provided. In addition, to generate the consecutive stable pulses at a repetition rate of 1 MHz, a time division multiswitch based sequential logic circuit was designed. This method ensures a minor disparity of the switch-ON time due to the multiple channels of the MOSFETs used in the circuit scheme. In the end, experimental tests were carried out to validate the design parameters.

II. Materials and Methods

A. Design of the Pulsed Power Supply

Briefly, the pulsed power supply is comprised of a capacitor charging dc power source, a capacitive filter chassis, MOSFET switching driver, and resistor and diode (RD) snubber circuit for diode, as demonstrated in Fig. 2(a). The fast switching of the MOSFETs generates the pulses, resulting in the step response of the circuit. To obtain a faster rise time and high peak current, the circuit was operated on the underdamping state (see Section II-B) by adjusting the value of capacitance. The snubber circuit is essential to avoid over-voltages due to the recovery current from the inductor and absorb surge voltage while turning off the MOSFETs.

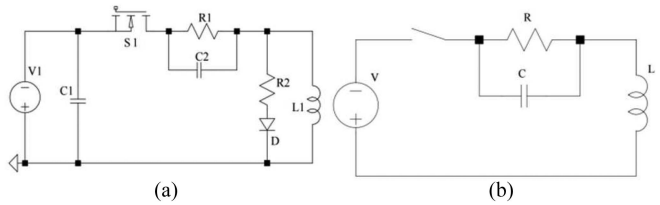

Fig. 2. (a) Working principle of the pulsed power supply and (b) equivalent circuit of the transient switching characteristics. Note that V is the voltage of the dc power source, S1 represents the MOSFET, while R, C, L, and D represents the resistance, capacitance, inductance, and diode, respectively.

B. Equivalent Circuit Analysis

In this section, a detailed mathematical derivation on the selection of the main parameters (peak current (i_L), charging voltage ($V_{\rm dc}$)) is provided. To simplify the calculation, an equivalent circuit of the transient switching characteristic of the pulsed power supply is given in Fig. 2(b).

The response of the system on the inductance load is described as a second-order differential equation in (1) based on the Kirchhoff's current law, here, assuming the initial conditions $i_L(0) = 0$ and $i_L^{\cdot}(0) = \frac{V}{L}$. Knowing the step response of the system evaluates the ability to reach one stationary state from the initial state, as well as the stability of such a system

$$\frac{d^2 i_L}{dt^2} + \frac{1}{RC}\frac{di_L}{dt} + \frac{1}{LC} i_L = \frac{V}{LRC} \tag{1}$$

where the discriminant can be expressed as

$$\Delta = \frac{1}{R^2 C^2} - \frac{4}{LC}. \tag{2}$$

The discriminant (Δ) of the nonhomogeneous second-order linear differential formula (1) corresponds to different damped states—namely, overdamping ($\Delta > 0$), critically damping ($\Delta = 0$), and underdamping states ($\Delta < 0$)—which indicate the different front-edge pulse of the circuit response, as described in Fig. 3 [formula is given in (6)]. It is known that the cross time of the electron beam bunches to the kicker is approximately 1.5 ns, thereof the flat-top width is approaching to 5 ns, assuming a front-edge jitter of the pulse of 1 ns. As a result, it is required to remain the underdamping state as the pulses oscillate through the equilibrium position, which demonstrate a faster rise time and a reduced width of the pulse waveform.

Based on the method of undetermined coefficients, the complementary solution is expressed as (3) under the underdamping state $\left(\Delta\langle 0,\ R\rangle \frac{1}{2}\sqrt{\frac{L}{C}}\right)$

$$i_L = e^{\alpha t}\left[N_1 \cos\left(\omega_d t\right) + N_2 \sin\left(\omega_d t\right)\right] + \frac{V}{R} \tag{3}$$

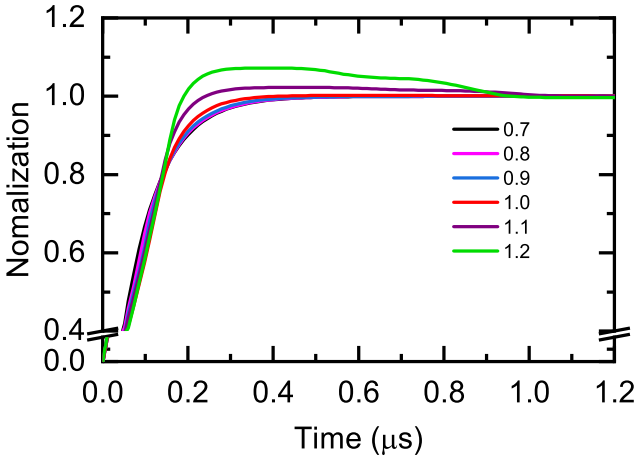

Fig. 3. Front-edge pulse waveform at varied damping coefficient.

where, $\alpha = -\frac{1}{2RC}$ represents the real number of the characteristic equation, while $\omega_d = \frac{\sqrt{\frac{4}{LC}-\frac{1}{R^2C^2}}}{2}$ denotes the imaginary number.

Substitute the initial conditions ($i_L(0) = 0$ and $\dot{i_L}(0) = \frac{V}{L}$) to the complementary solution [formula (3)], N_1 and N_2 values are obtained $N_1 = -\frac{V}{R}$, $N_2 = \frac{\frac{V}{L}+\frac{V\alpha}{R}}{\omega_d}$).

Eventually, the complementary solution of (1) can be written as

$$i_L = e^{\alpha t}\left[-\frac{V}{R}\cos(\omega_d t) + \frac{\frac{V}{L}+\frac{V\alpha}{R}}{\omega_d}\sin(\omega_d t)\right] + \frac{V}{R}. \quad (4)$$

In the next step, the voltage of the capacitor is calculated. The differential equation on the voltage of the capacitor is given in (5), the Laplace transform is adopted to simplify the mathematical analysis

$$\frac{d^2u_c}{dt^2} + \frac{1}{RC}\frac{du_c}{dt} + \frac{1}{LC}u_c = \frac{u_s}{LC} \quad (5)$$

$$\sigma = \frac{1}{2R}\sqrt{\frac{L}{C}} \quad (6)$$

$$\omega_d = \omega_n\sqrt{1-\sigma^2} \quad (7)$$

$$\omega_n = \sqrt{\frac{1}{LC}} \quad (8)$$

where σ is the damping coefficient, ω_d is the underdamped natural angular frequency, while ω_n is the natural frequency. The characteristic equation of (5) is converted as (9) using Laplace transform

$$S^2 + 2\sigma\omega_n S + \omega_n^2 = 0. \quad (9)$$

The step response in the frequency domain is given in (10), and the time domain function can be converted back by using the inverse Fourier transform, as shown in (11)

$$C(S) = \frac{1}{S} * \frac{\omega_n^2}{S^2 + 2\sigma\omega_n S + \omega_n^2}$$

$$= \frac{1}{S} - \frac{S+\sigma\omega_n}{(S+\sigma\omega_n)^2+\omega_d^2} - \frac{\sigma\omega_n}{(S+\sigma\omega_n)^2+\omega_d^2} \quad (10)$$

$$C(t) = 1 - e^{-\sigma\omega_n t}\cos\omega_d t - \frac{\sigma}{\sqrt{1-\sigma^2}}e^{-\sigma\omega_n t}\sin\omega_d t$$

$$= 1 - \frac{1}{\sqrt{1-\sigma^2}}e^{-\sigma\omega_n t}\sin(\omega_d t + \beta) \quad (11)$$

where $\cos\beta = \sigma$, $\sin\beta = \sqrt{1-\sigma^2}$.

As a result, the time transient at the peak voltage of the capacitor can be derivated, as shown in (12). Given the fact that the variations of the voltage at the given time equal to 0, ultimately, the peak time transient value (t_c) is obtained in (14) by combing (12) and (13) as follows:

$$\tan(\omega_d t + \beta) = \frac{\sqrt{1-\sigma^2}}{\sigma} = \tan\beta \quad (12)$$

$$\omega_d t_c = n\pi \quad (13)$$

$$t_c = \frac{\pi}{\omega_d} = \frac{2\pi}{\sqrt{\frac{4}{LC}-\frac{1}{R^2C^2}}}. \quad (14)$$

For the time-domain analysis, the phase shift of inductor (t_i) relative to t_c is β ($\cos\beta = \sigma$), therefore, the peak time transient of the inductor is calculated in

$$t_i = \frac{\pi-\beta}{\omega_d} = \frac{2(\pi-\beta)}{\sqrt{\frac{4}{LC}-\frac{1}{R^2C^2}}}. \quad (15)$$

Substitute (15) back to (4), the peak current of the inductor (i_L) can be expressed as (16). It can be seen that the peak current is in proportional to the charging voltage, which allows for easier regulation of the kicker deflecting angle

$$\mathrm{i_L} = \mathrm{V}\sqrt{\frac{\mathrm{C}}{\mathrm{L}}}\cdot \mathrm{e}^{-\frac{\sigma(\pi-\beta)}{\sqrt{1-\sigma^2}}} + \frac{\mathrm{V}}{\mathrm{R}} \quad (16)$$

where $\sigma = \frac{1}{2R}\sqrt{\frac{L}{C}}$, $\cos\beta = \sigma$.

Overall, the evolution of the function can help with the circuit design and aid the selection of the main parameters. A trade-off needs to be made between the leading-edge time and the flat-top width of the pulsed power supply.

C. DC Power Supply

A commercial off-the-shelf capacitor charging power supply (MagnaDC, DBx Modul TSD1000-15, USA) is used to charge the capacitor [see Fig. 2(a)] at an output voltage of 1 kV, current up to 15 A, and high stability of 0.001%. This power supply was chosen due to its readily availability, and the optimum conditioning capacitor to minimize the turn-ON oscillations.

Given the remarkably high repetition rate of the pulsed power supply (1 MHz), a capacitor was connected in parallel at the end of dc power supply. The capacitance was calculated via (17), assuming the amplitude variations of the energy for 200 pulses

are constrained within 0.01%

$$\frac{1}{2}C \cdot V^2 - \frac{1}{2}C(99.99\% \cdot V)^2 = \sum_{1}^{200}(Q) \tag{17}$$

where Q represents the discharged energy per pulse, C represents the capacitance of the capacitor, and V is the voltage.

Six metalized thin-film capacitors ($C = 2.5$ mF, $V = 1.25$ kV) were connected in parallel to achieve a total capacitance of 15 mF. These capacitors were chosen due to their high insulated resistance, low equivalent series resistance, low self-inductance, and hence, low dissipation loss. Moreover, during a breakdown caused by the transient voltage stress, the heat generated by the arcing evaporates the metalized thin film, thereby removing and isolating the occurrence of a short circuit. This self-healing property ensures the reliable operation of the dc power unit.

D. MOSFET Switching

Transient voltage is induced during fast turn-OFF, which can cause the failure of the switching elements. To cope with the high power switching applications, SiC MOSFET was selected due to its low on-state resistance, lower leakage current at high temperatures, and hence, low power dissipation. Eight MOSFETs (C2M0045170P, Wolfspeed) were employed—comprised of four channels with two MOSFETs connected in parallel per channel—which switch in a sequential order (1 μs of difference) to generate the output pulses. Each channel is in response to occupy one-quarter of the repetition rate (250 kHz). This has posed a challenge to the design of the sequential logic of the clock pulses (CP) at 1 MHz. It is aware that the CP signal is defined by the accelerator timing system, which exhibits a pulse width of 200–700 ns, with a minimum step of 4 ns and a jitter less than 100 ps.

The typical design of the CP is based on the D flip–flops that capture the rising edge of the clock. Thereafter the front-edge jitter is introduced due to the varied states of different routes of the clock signals ($Q0$–$Q3$). In this design, a fixed time delay ($\Delta\tau$) is introduced to the original CP signal (CP+$\Delta\tau$), and the logical conjunction is then implemented with the four routes of clock signals to reduce the leading-edge jitter, as specified in the equations of state in (18). The sequential logic waveform of the clock pulses is provided in Fig. 4 for a further demonstration

$$\begin{cases} Q_3^{n+1} = CP\overline{Q_3}Q_2\overline{Q_1} \\ Q_2^{n+1} = CPQ_3\overline{Q_1} \\ Q_1^{n+1} = CP\overline{Q_3}Q_2\overline{Q_1} \\ Q_0^{n+1} = Q_1. \end{cases} \tag{18}$$

In the sequential logic circuit, the clock signal is distributed to all the memory elements. The output of the flip–flop only changes when triggered by the CP, and hence, the changes to the logic signals start at regular intervals and synchronized by the clock. The state of the synchronous circuit only changes with the CP, which determines the switch-ON time of the MOSFETs. The electrical schematic of the sequential circuit is given in Fig. 5.

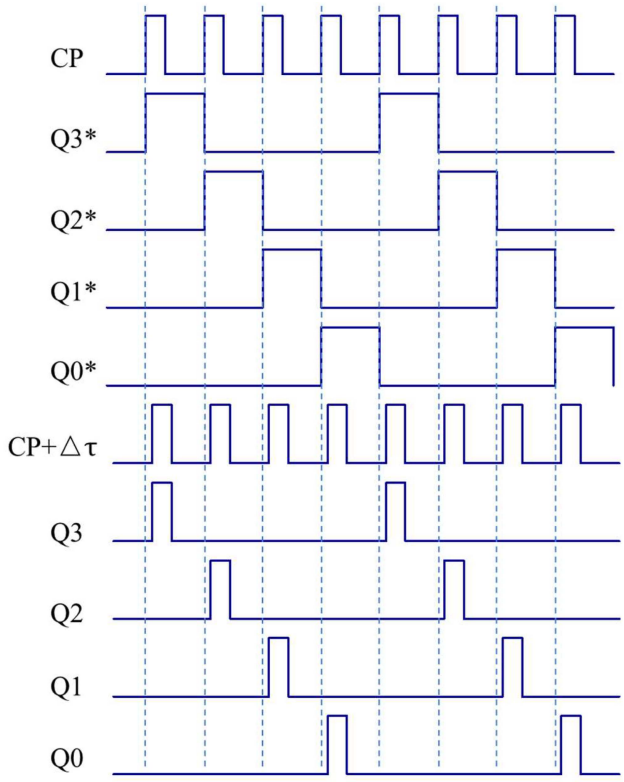

Fig. 4. Waveform of the sequential logic for the clock pulses.

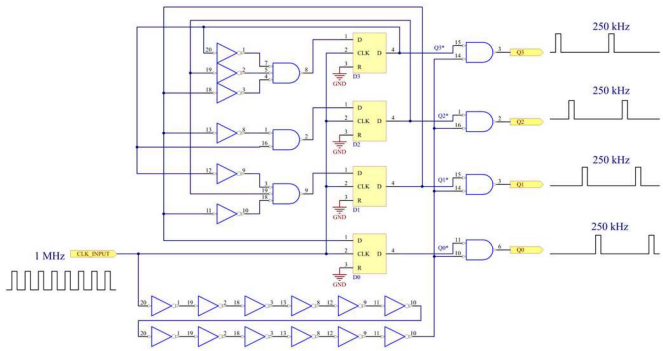

Fig. 5. Sequential circuit prior to the MOSFETs driver used in the pulsed power supply.

The driver modules are powered by a power element (VRB1224ZP-6WR) with a maximum isolated voltage up to 1.5 kV, and the optical fiber is utilized for isolation to reduce the interference during discharge period. The drive circuit is stabilized on the negative polarity of the bus voltage, which offers protection features and improves the switching characteristics of the MOSFETs. Based on the abovementioned analysis, the choices of the main parameters were summarized in Table II, while the simulated current graph based on the mathematical derivations was drawn at varied voltages in Fig. 6 to give a clear overview (indicators are marked). The voltages at 750 V and 590 V were selected as they represented the maximum charging voltage, and required voltage for the actual load in the experiments (see Section III).

TABLE II
SELECTIONS OF THE MAIN PARAMETERS IN THE PULSED POWER SUPPLY [SEE SYMBOLS IN FIG. 2(A)]

Parameters	Value
Resistor R1 (Ω)	14
Capacitor C2 (nF)	4
Resistor R2 (Ω)	25
Capacitor C1 (mF)	15
SiC MOSFET (N-channel)	8*C2M0045170P
Diode D1	C3D25170H
Dc voltage (V_{dc})	-750
Kicker inductance L1 (μH)	1.6

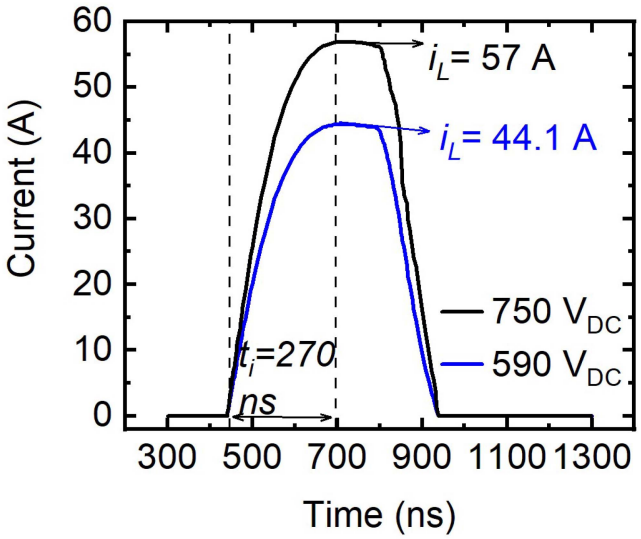

Fig. 6. Calculated pulse current of the inductor at varied voltages. t_i is the transient time at peak current, while i_L is the peak inductor current.

E. Experimental Measurements

Measurements were taken to quantify the flat-top width, pulse-to-pulse stability, rise and fall time of the output waveform. Briefly, a digital oscilloscope (Rohde and Schwarz, RTE1104, Germany)—1 GHz bandwidth, sampling rate of 5 Gs/s per channel, 16 bit vertical resolution—was utilized for visualizing the output pulses. A signal generator (Tektronix, AFG3022B, USA) was used to generate two signals, one being triggered for the pulsed power supply and the other for the oscilloscope used as synchronous sample signal. The pulsed current measurements were made via a wide-band current monitor (Pearson, 6600, USA) at a sensitivity of 0.1 V/A, root-mean-square current up to 40 A, bandwidth from 25 Hz to 120 MHz.

III. RESULTS AND DISCUSSIONS

A. Thermal Analysis

In this section, a detailed thermal analysis is executed to characterize the physical properties of the pulsed power supply under conditions that simulate the real working environment. It allows to find the temperature distribution, heat gradient and flowing, which in turn to help distinguish the power loss among varied components.

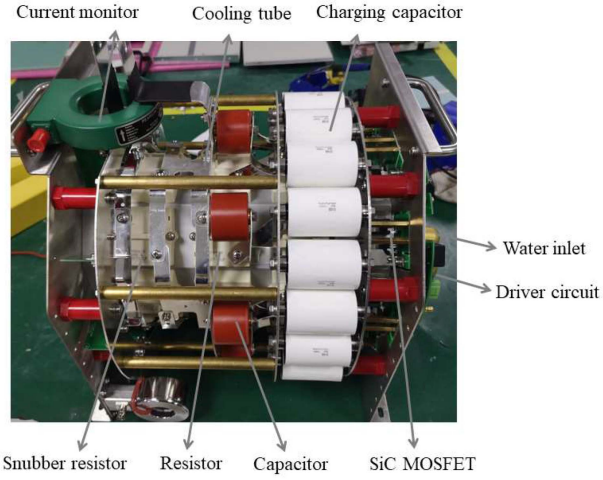

Fig. 7. Picture of the pulsed power supply, demonstrating the crucial components.

TABLE III
THERMAL SIMULATION OF THE ALUMINIUM PLATE SHEET ALLOY, HERE ΔT REPRESENTS THE TEMPERATURE INCREASE, AND ΔP REPRESENTS THE PRESSURE DROP ACROSS THE PLATE

Flowrate (L/min)	Inlet T (°C)	ΔT (°C)	T_{max} (°C)	ΔP (pa)
6	20	26	91.2	295.6
8	20	19.5	84	461
10	20	15.6	79.2	665
12	20	13	75.8	908
14	20	11.2	73.1	1189
20	20	8.5	69.1	2268
30	20	5.6	60.4	2839

Here, the 3A21 aluminium plate sheet alloy is used due to its good weldability, high corrosion resistance and intensity. It has a thermal conductive coefficient of 180 W/m·K. Thermally conductive silicon grease is applied with a thickness of 0.15 mm at a conductive coefficient of 2 W/m·K, while deionized water is used for thermal dissipation of the pulsed power supply. A photo of the pulsed power supply is given in Fig. 7 to have a clear overview of the main components, while the power dissipation is analyzed in the following section, assuming an inlet water temperature of 20 °C at a water velocity of 1 m/s. It is noted that the natural convection of the air and thermal radiation are both ignored. The thermal simulation is given in Fig. 8 (crucial components were marked) via using Ansys 15.0, while the maximum temperature and pressure drop across the plate is indicated in Table III.

Intuitively, the high flowrate leads to less increase of the temperature, whereas a high pressure drop across the plate sheet is created. In order to make a tradeoff between cooling capacity and induced pressure drop, a flowrate of 26 L/min is selected at the end. As a result, at an ambient temperature of 20 °C, the rise of temperature of 6.5 °C at the water outlet side is observed. The heat and power dissipation among the varied components (represented by different colors) are shown in Fig. 9, while the power loss is summarized in Table IV for further comparison. It is aware of that most of the power loss eventually becomes heat inside a component.

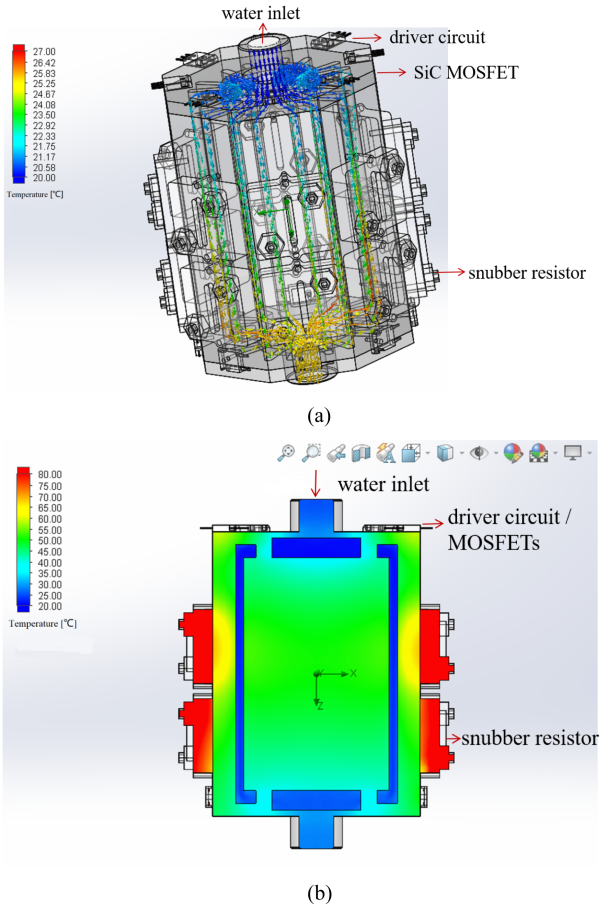

Fig. 8. Thermal simulation of the pulsed power supply, demonstrating (a) water trajectory, and (b) temperature distribution.

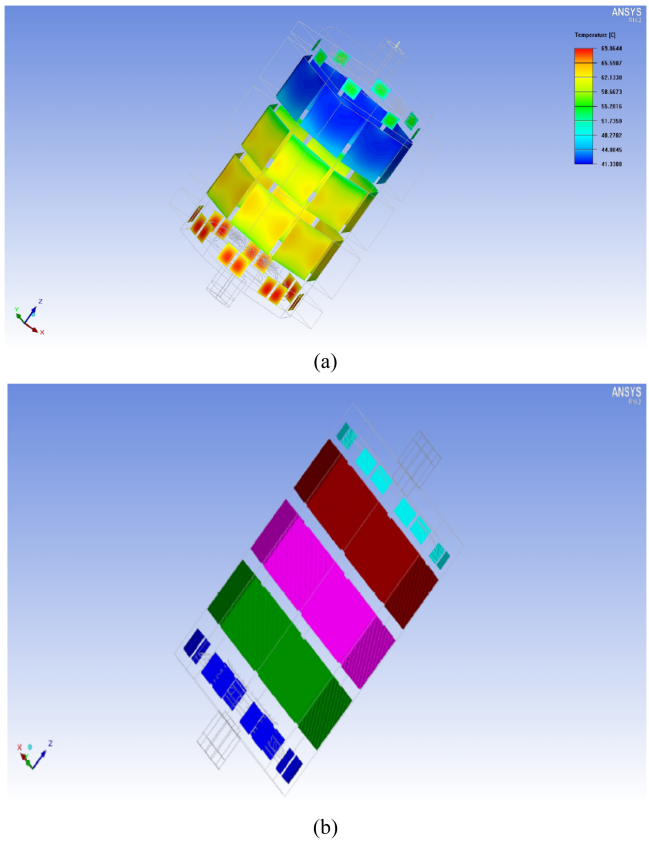

Fig. 9. (a) Temperature gradient of the crucial components, and (b) power dissipating components of the pulsed power supply.

TABLE IV
POWER DISSIPATION OF THE PULSED POWER SUPPLY, THE COLOR REPRESENTS VARIED COMPONENTS, AS SHOWN IN FIG. 9

Thermal source	Color	Quantity	Power loss per unit (W)	Sum (kW)
Diode of snubber circuit	Cyan	8	125	1
Resistor of snubber circuit	Red	8	125	1
Resistor	Magenta	8	500	4
Resistor	Green	8	500	4
MOSFET	Blue	16	125	2

Referring to Table IV, it demonstrates a total power loss of approximately 12 kW. Generally, the ON-resistance value of the MOSFET increases at high temperatures due to its thermal dependency, which alternatively reduces the switching performance. The total dissipated power of the MOSFET is relatively low (∼17%) mainly due to the small duty cycle. The water cooling is provided to maintain the temperature of the transistors and gate drivers, and thus reducing the slow thermal drift. The snubber circuit consumes ∼17% of the total power loss, and it is beneficial to decrease the temperature to minimize the stray inductance of the circuit. It needs to be noted that the suppressing surge capability of the RD snubber is limited due to the lack of a capacitor, and a surge voltage (drain-to-source voltage, V_{DS}) of 1.1 kV was observed while turning off the MOSFET. An improved RCD snubber circuit, aiming for a switching loss decline of ∼10% would be substituted shortly. It can be seen that the power dissipation of the resistors accounts for 75% of the total power loss. Consequently, the critical measure is to reduce the heat dissipation of these parasitic loads of the pulsed power supply. A feasible solution is to migrate all the components to the cooling plate so as to decrease the power consumption, whereas a mechanical modification is necessary for the future design.

B. Waveform

To verify the design requirement, the output pulses with nine cycles at an interval of 1 μs were measured by using the method discussed in Section II-E [displayed in Fig. 10(a)]. A peak-to-peak voltage of 4.41 V and a repetition rate of 1 MHz was obtained. As shown in Fig. 10(b), the pulse shape is close to half-period of sine function with zero-to-zero duration of ∼600 ns. The visually observed rise time indicates a value of ∼160 ns and with a fall time of ∼164 ns. The maximum amplitude reached approximately 4.41 V (equal to 44.1 A as in current) once connecting with the magnet (load in this case) and operated at 1 MHz. And the measured full-width-at-half-maximum was ∼396 ns. Due to the different charging voltage ($V_{\rm dc}$) used in the experiment, a variation of the peak inductor current exists between the experimental results and simulations

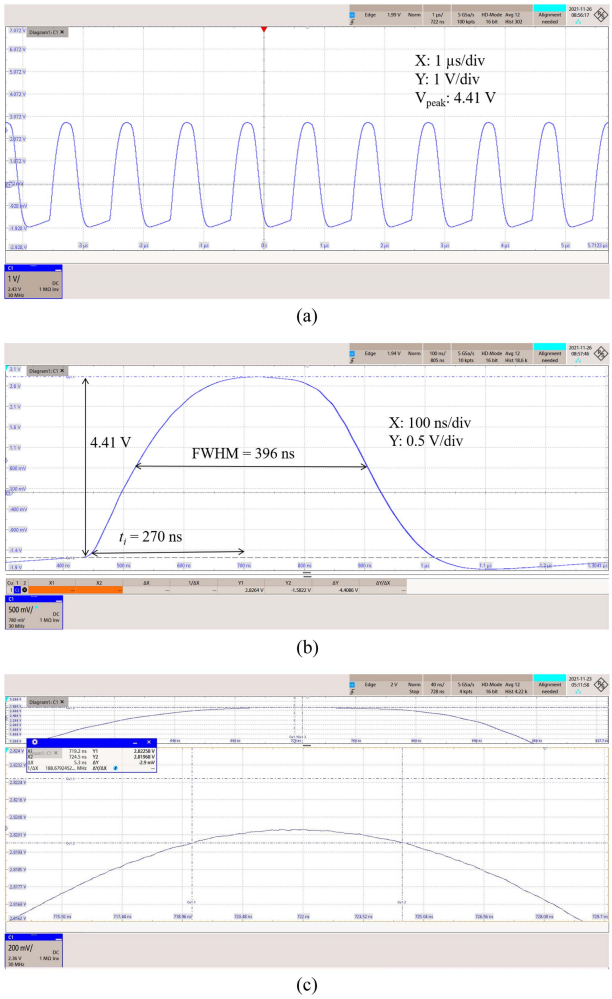

Fig. 10. Output waveform of the pulsed power supply, showing (a) consecutive output pulses at 1 MHz, (b) single pulse shape, and (c) flat-top width.

when substituting the presented values in Table II. The transient time (t_i) at peak current was calculated to be 270 ns, while peak current was 57 A at a maximum voltage of 750 V (see Fig. 6). Comparatively, the peak current was deliberately constrained up to 44.1 A at a lower rating voltage of 590 V as it yet satisfied the demand of the magnet in the real applications (determined by the deflecting angle to the beam), resulting in a rising time (10–90%) of ∼160 ns. Whereas an identical transient time of 270 ns can be observed, which is in corresponding to the simulation. An expanded view of the pulse flat-top was given in Fig. 10(d), where a flat-top width of 5.3 ns (@99.99%) was observed. Overall, the experimental results are well correspondent in terms of peak current and transient time. A variation of the back-edge pulse was observed owing to the distributed parameters of the snubber circuit, whereas, it has trivial impacts on the kicker magnets and, thus, is not detailed.

Nevertheless, the biggest challenge appears to be the lead connections caused by the distributed parameters when connecting with the load (magnet), which may lead to the distortion of the pulse shape. This issue is required to be investigated in the future work.

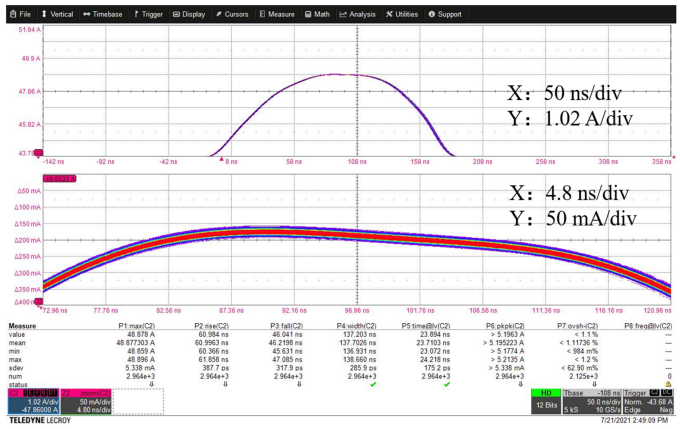

Fig. 11. Stability test of the pulsed power supply at high repetition rate of 1 MHz within 3 min.

C. Pulse-to-Pulse Amplitude Stability

It is difficult to measure the stability of the pulsed power supply to a sub-10^{-4} level with standard current transducers. A high precise measurement system was used to evaluate the amplitude stability (see Section II-E). It is capable of measuring the amplitude stability down to around 10 ppm. The measurement is displayed in Fig. 11, where a multiple pulses (3 min of 1 MHz operation) is plotted, exhibiting a pulse-to-pulse amplitude stability of 108 ppm (estimated by the ratio of standard deviation and peak value). Given the fact that the operation of the pulsed power supply on a repetition rate of 1 MHz was primarily achieved by actively switching the four channels in a time-based mode, this leads to a negative effect on the consistency of the ON-states. It is known that the switching performance of the MOSFET is mainly determined by the dv/dt and switching loss [24]. As the temperature rises from 25 °C to 125 °C, the *dv/dt* and switching loss indicate an increase of ∼14% and 6%, respectively [24], [25]. The deterioration of the switching loss may cause fluctuations in the pulses. Notably, the stability of the pulsed power supply demonstrated a reduction of 0.05% when the temperature approached 65 °C, which highlights the significance of sufficient thermal design. It is anticipated to bounce back to ∼0.01% once it reaches thermal equilibrium. The trivial influences on the pulse and flat-top width are neglected. A pulse-to-pulse amplitude stability below 100 ppm remains an obstacle at this stage.

IV. Conclusion

In this work, the prototype of a pulsed power supply for the kicker magnet at a high repetition rate of 1 MHz was designed for the SHINE facility. The design was based on *LRC* second-order circuit that enables a fast pulse forming scheme, while a systematic mathematic method was derivated and guided for the circuit design. The experimental results indicated a peak pulse current of approximately 44.1 A at a repetition rate of 1 MHz with an inductive load of 1.6 μH. Whereas, the pulse-to-pulse amplitude stability reached around 108 ppm during a short-term test of 3 min at a flat-top width of 5.3 ns. To assure an accurate trajectory of the beam bunches to the undulators, further

study is underway to improve the pulse-to-pulse stability below 100 ppm of the pulsed power supply. A charging power supply at a stability of 100 ppm and a larger capacitor were employed to stabilize the busbar voltage. Moreover, eight MOSFETs were connected in parallel to allow a more consistent switching during the turn-ON states at 1 MHz.

Several measures are adopted to improve the performance of the pulsed power supply, including i) an improved snubber circuit based on RCD would be implemented to optimize the flat-top and the back-edge waveform by easily tuning the parameters. The switching loss is anticipated to be reduced as the snubber capacitor absorbs the energy stored in the inductance and clamps surge voltage while the MOSFET turns OFF; ii) a short circuit protection is applied to avoid overvoltage and short circuit faults to assure robust operating during fast switching.

ACKNOWLEDGMENT

The authors would like to thank Prof. H. Matsumoto, Prof. R. Bissonnette, Prof. L. Shang, and Prof. J. Chen for fruitful discussions. L.-S. Xiao is thanked for providing technical support.

REFERENCES

[1] M. Altarelli, R. Brinkmann, and M. Chergui, "The European X-ray free-electron laser technical design report," Hamburg, Germany, Tech. Rep. DESY-2006-097, Jul. 2007.
[2] B. E. Carlsten, "Tutorial on X-ray free-electron lasers," *IEEE Trans. Plasma Sci.*, vol. 46, no. 6, pp. 1900–1912, Jun. 2018, doi: 10.1109/TPS.2018.2827301.
[3] N. Huang, H. Deng, B. Liu, D. Wang, and Z. Zhao, "Features and futures of X-ray free-electron lasers," *Innovation*, vol. 2, no. 2, Mar. 2021, Art. no. 100097, doi: 10.1016/j.xinn.2021.100097.
[4] M. Paraliev and C. Gough, "Resonant kicker system with sub-part-per-million amplitude stability," in *Proc. Int. Part. Accel. Conf.*, 2017, pp. 3174–3177.
[5] C. Kondo et al., "High-precision pattern power supply of kicker magnet for multi-beamline operation at SACLA," in *Proc. Int. Part. Accel. Conf.*, 2017, pp. 3404–3407.
[6] K. Tono, T. Hara, M. Yabashi, and H. Tanaka, "Multiple-beamline operation of SACLA," *J. Synchrotron Radiat.*, vol. 26, pp. 595–602, Mar. 2019, doi: 10.1107/S1600577519001607.
[7] W. Decking and F. Obier, "Layout of the beam switchyard at the European XFEL," in *Proc. 11th Eur. Part. Accel. Conf.*, 2008, pp. 2163–2165.
[8] J. Rossbach, J. R. Schneider, and W. Wurth, "10 years of pioneering X-ray science at the Free-Electron Laser FLASH at DESY," *Phys. Rep.*, vol. 808, pp. 1–74, 2019, doi: 10.1016/j.physrep.2019.02.002.
[9] T. Beukers, M. Nguyen, and T. Tang, "Discrete element transmission line beam spreader kickers for LCLS-II," in *Proc. IEEE Int. Power Modulator High Voltage Conf.*, 2018, pp. 151–155, doi: 10.1109/IPMHVC.2018.8936755.
[10] G. Jiang et al., "The cryogenic control system of SHINE," *EPJ Techn. Instrum.*, vol. 8, Jul. 2021, Art. no. 11, doi: 10.1140/epjti/s40485-021-00066-7.
[11] M. Dehler and G. Behrmann, "Stripline devices for Flash and European XFEL," in *Proc. 13th Beam Instrum. Workshop*, 2008, pp. 110–114.
[12] M. Paraliev and C. Gough, "Towards sub-ppm shot-to-shot amplitude stability of SwissFEL resonant kicker," in *Proc. IEEE Int. Power Modulator High Voltage Conf.*, 2016, pp. 246–249, doi: 10.1109/IPMHVC.2016.8012863.
[13] M. Paraliev and C. Gough, "Comparison of high resolution 'balanced' and 'direct conversion' measurement of SwissFEL resonant kicker amplitude," in *Proc. IEEE Pulsed Power Conf.*, 2015, pp. 1–4, doi: 10.1109/PPC.2015.7297016.
[14] J. J. Shea, "Advances in high voltage engineering [Book Review]," *IEEE Elect. Insul. Mag.*, vol. 23, no. 1, Jan./Feb. 2007, Art. no. 53, doi: 10.1109/MEI.2007.288471.
[15] G. A. Mesyats, "Pulsed systems: Design principles," in *Pulsed Power*, 1st ed. Berlin, Germany: Springer, 2005, pp. 13–14.
[16] Y.-F. Liu, H. Matsumoto, M. Gu, G.-Q. Li, and S. Li, "Design of an oil-immersed pulse modulator for X-Band 50-MW klystron," *IEEE Trans. Plasma Sci.*, vol. 51, no. 3, pp. 802–807, Mar. 2023, doi: 10.1109/TPS.2023.3248094.
[17] T. Shintake and T. Inagaki, "Compact klystron modulator for XFEL/SPRING-8," in *Proc. Int. Part. Accel. Conf.*, 2010, pp. 3287–3289.
[18] X. Yuan, I. Laird, and S. Walder, "Opportunities, challenges, and potential solutions in the application of fast-switching SiC power devices and converters," *IEEE Trans. Power Electron.*, vol. 36, no. 4, pp. 3925–3945, Apr. 2021, doi: 10.1109/TPEL.2020.3024862.
[19] C. Langpoklakpam et al., "Review of silicon carbide processing for power MOSFET," *Crystals*, vol. 12, no. 2, Feb. 2022, Art. no. 245, doi: 10.3390/cryst12020245.
[20] W. Zeng et al., "A novel high frequency bipolar pulsed power generator for biological applications," *IEEE Trans. Power Electron.*, vol. 35, no. 12, pp. 12861–12870, Dec. 2020, doi: 10.1109/TPEL.2020.2994333.
[21] Y. He et al., "10MHz high-power pulse generator on boost module," *IEEE Trans. Ind. Electron.*, vol. 68, no. 7, pp. 6286–6296, Jul. 2021, doi: 10.1109/TIE.2020.2994860.
[22] Y. Mi, N. Xu, J. Chen, and Z. Li, "High-frequency bipolar solid-state LTD based on a self-triggering H-bridge," *IEEE Trans. Power Electron.*, vol. 37, no. 5, pp. 5898–5907, May 2022, doi: 10.1109/TPEL.2021.3131251.
[23] Y. Mi, C. Bian, P. Li, C. Yao, and C. Li, "A modular generator of nanosecond pulses with adjustable polarity and high repetition rate," *IEEE Trans. Power Electron.*, vol. 33, no. 12, pp. 10654–10662, Dec. 2018, doi: 10.1109/TPEL.2018.2805820.
[24] S. Ji, S. Zheng, F. Wang, and L. M. Tolbert, "Temperature-dependent characterization, modeling, and switching speed-limitation analysis of third-generation 10-kV SiC MOSFET," *IEEE Trans. Power Electron.*, vol. 33, no. 5, pp. 4317–4327, May 2018, doi: 10.1109/TPEL.2017.2723601.
[25] Wolfspeed, "Silicon carbide power MOSFET technology N-channel enhancement mode," Dec. 2022. [Online]. Available: https://assets.wolfspeed.com/uploads/2020/12/C2M0045170P.pdf

Yong-Fang Liu (Member, IEEE) was born in Shandong Province, China, in 1987. He received the Ph.D. degree in nuclear technology and application from the University of Chinese Academy of Sciences, Beijing, China, in 2020.

His research interests include pulsed power supply and pulsed magnet technology, such as pulsed klystron modulators, linear transformer drivers, particle accelerator injection and extraction magnet, particle accelerator beam distribution magnet, and irreversible electroporation pulsed power supply.

Ming Gu received the B.S. degree in applied physics from the University of Science and Technology of China, Hefei, China, in 1982.

He is currently a Full Professor with the Shanghai Advanced Research Institute, Chinese Academy of Sciences, Beijing, China. His research interest includes particle accelerator technologies.

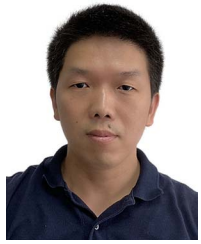

Qi-Bing Yuan received the Ph.D. degree in nuclear technology and application from the University of Chinese Academy of Sciences, Beijing, China, in 2008.

He was with the Shanghai Institute of Applied Physics in 2003 and subsequently was with the Shanghai Advanced Research Institute in 2018. He is currently the leader of the group of pulsed technology, magnet, and power supply technology division. His research interests include injection and extraction technology of synchrotrons and beam switchyard technology for the FEL facility.

Ruiping Wang received the B.S. and M.S. degrees in electrical engineering from Xi'an Jiaotong University, Xi'an, China, in 2003 and 2006, respectively.

Her research interests include high-voltage pulsed power supply, special magnets, and precision motion control.

Jin Tong received the Ph.D. degree from the University of Chinese Academy of Sciences, Beijing, China, in 2021.

His specialty relies on Nuclear Technology and Application. He mainly engaged in the design of pulse magnets and magnetic measurement systems for electron beam injection and extraction systems over the years. His current research interests include linear/nonlinear kicker magnets, eddy current septum magnets, and Lambertson magnets.

Sheying Li received the Ph.D. degree in electrical engineering from Karlsruhe Institute of Technology (KIT), Karlsruhe, Germany, in 2022.

She is currently with the group of pulse power supplies with Shanghai Advanced Research Institute, Chinese Academy of Sciences, Beijing, China. Her research interests mainly include photovoltaic technology for water treatment, energy storage technology, energy management control, and dynamic system control for pulsed power supply.